SAND2018-14318R

Sandia National Laboratories
Albuquerque, New Mexico 87185

date: December 20, 2018

to: Distribution

from: Edmundo Corona (1554), Amanda Jones (1528) and Jennifer Rees (1554)

subject: FY18 Thermal Mechanical Failure: SS-304L calibration, Taylor-Quinney parameter measurement and kinematic hardening plasticity.

The Thermal-Mechanical Failure project conducted in FY 2018 was divided into three subprojects:

1. Calibration of the uniaxial response of 304L stainless steel specimens at three temperatures (20, 150 and 310°C) and two strain rates (2×10^{-4} and 8×10^{-2} s^{-1}).
2. Measurements of the fraction of plastic work that is converted to heat (Taylor-Quinney parameter) for 304L stainless steel. This fraction is usually assumed to be 0.95 in analysis because data is only available for a few materials.
3. Comparison of the predicted responses by isotropic and kinematic hardening plasticity models in a couple of simplified structural problems. One problem is a can crush followed by pressurization and is loosely associated with a crush-and-burn scenario. The other problem consists of a drop scenario of a thin-walled cylinder that carries a cantilevered internal mass.

1 Rate and Temperature Calibration for 304L Stainless Steel.

The objective of this part of the project was to attempt calibration of relatively simple plasticity models for 304L stainless steel that take into account both rate and temperature dependece of the material response. A set of material tests was conducted in the Structural Mechanics Laboratory (Jones, 2018). In these tests, flat uniaxial tension test specimens with test section nominal dimensions 1.25 in. by 0.375 in. by 0.060 in. were pulled at three nominal temperatures: 25, 150 and 310°C. The tests at 25 and 310°C were conducted at two strain rates: 2×10^{-4} s^{-1} and 8×10^{-2} s^{-1}. The test at 150°C was carried out only at the slower strain rate. The strain in the specimens was measured using an extensometer with 0.5 in. gage length while a load cell outside the oven measured the load. In addition,

thermocouples measured the ambient oven temperature as well as the temperature of the specimen at the edges and center of the test section. See Jones (2018) for more information regarding the test set-up.

Figure 1 shows the experimentally obtained engineering stress-strain curves at the three tempearatures and slower strain rate in solid lines. Clearly, the strength and engineering strain to failure decreased with increasing temperature. The decrease in failure engineering strain is characteristic of this material in the temperature range shown. At higher temperatures, the engineering strain at failure increases as demonstrated in experiments by Bonnie Antoun (8343). Also note the slight serrations on the curve at 310°C.

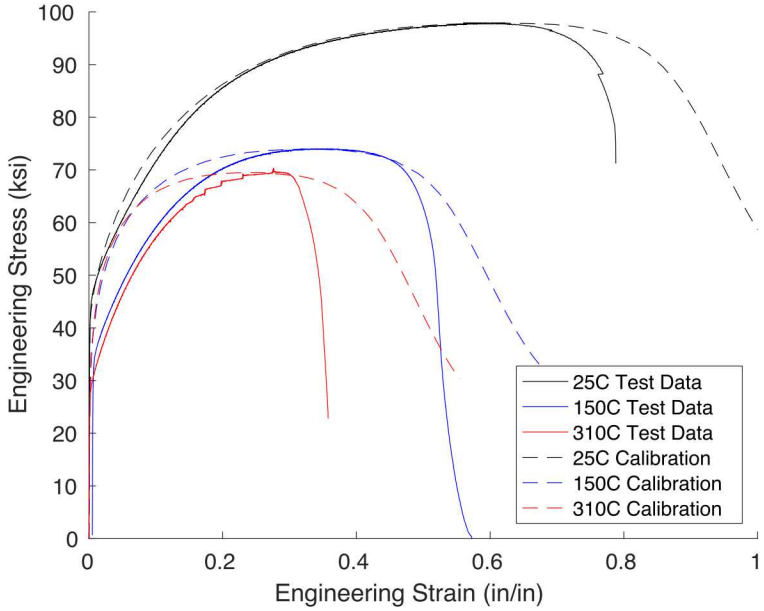

Figure 1: Measured engineering stress-strain curves for 304L stainless steel at three tempeartures and strain rate of 2×10^{-4} s^{-1} shown in solid line. Results of the calibrated power-law hardening model are shown dashed.

The start of the plasticity calibration process is to choose a model to represent the hardening function of the material within a J_2, isotropic hardening model. Following previous work (Corona and Lester, 2017), a power-law hardening model where the hardening function is given by

$$H = A + B(\varepsilon_t^p)^n, \tag{1}$$

and A, B and n are the material parameters, seems reasonable. The stress-strain curve at each temperature with the slow strain rate was fitted separately, so A, B and n are functions of temperature. The measured temperature showed essentially isothermal conditions during the tests. The values of the parameters at each temperature were found using a systematic trial-and-error procedure. The parameter values are given in Table 1, and Fig. 1 shows the resulting engineering stress-strain curves in dashed line. Since the shape of the hardening

Table 1: Values of power-law hardening models at three temperatures.

T, °C	A, ksi	B, ksi	n
25	40	189	0.635
150	20	121	0.345
310	7	113	0.230

curve is constrained by (1), it was difficult to reproduce the shape of the measured curves over the whole strain rage. Compromises were made, especially for the two cases at high temperature, to try to have the ultimate stress occur at about the same strain as in the tests. These compromises led to gaps between tests and simulations that can be seen at strains below 0.2.

The effect of strain rate on the measured stress-strain curves can be seen in Figs. 2(a) and 3(a). The measured curves, in solid lines, are compared for the slow and fast loading rates at 25 and 310°C, respectively. The effect of strain rate seems more pronounced at 25°C. Here, the yield stress increased, but the strain at the ultimate stress decreased for the higher strain rate test compared to the slow one. At 310°C, increasing the strain rate essentially did not influence the yield stress, and only influenced the strain at ultimate stress a little. Note that the serrations disappeared at the faster strain rate and the post-ultimate response dropped less precipitously. Figures 2(b) and 3(b) show the increase in temperature measured at the center of the test section in solid line for the higher strain rate tests. It is more pronounced in the 25°C test.

To explore a possible way to model the test observations for temperature and strain rate effects in the uniaxial tension tests, a simple material point model was constructed. This model is valid only up to the ultimate stress point since it does not consider the neck that develops in the test specimens past the ultimate stress point.

The description of the model starts with the expression between the true strain (ε_t) and engineering strain (ε_e), which is given by

$$\varepsilon_t = \ln(1 + \varepsilon_e). \tag{2}$$

As is customary, the true strain increment is additively decomposed into an elastic and a plastic part

$$d\varepsilon_t = d\varepsilon_t^e + d\varepsilon_t^p. \tag{3}$$

The relation between the true and engineering stress is given by

$$\sigma_t = \sigma_e(1 + \varepsilon_e). \tag{4}$$

The true stress is given by the product of two functions

$$\sigma_t = HR \tag{5}$$

where

$$H = H(\varepsilon_t^p, T) = A(T) + B(T)(\varepsilon_t^p)^{n(T)}, \tag{6}$$

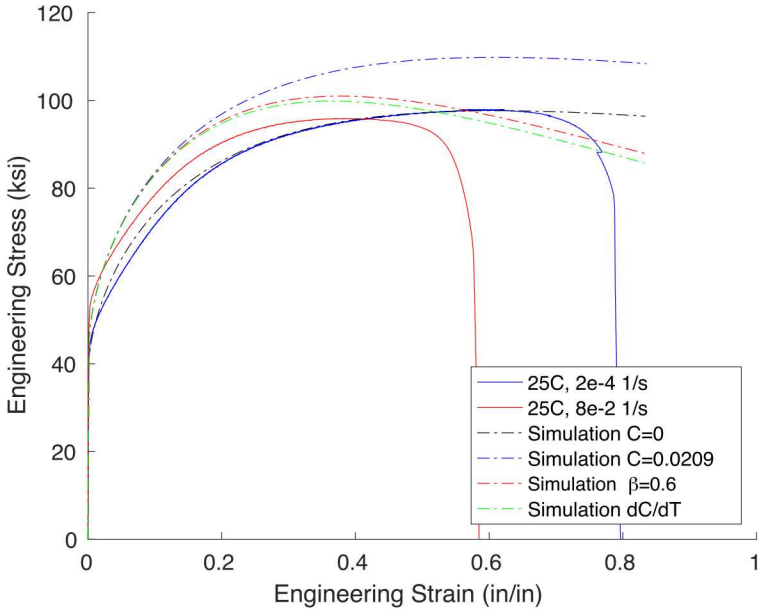

(a)

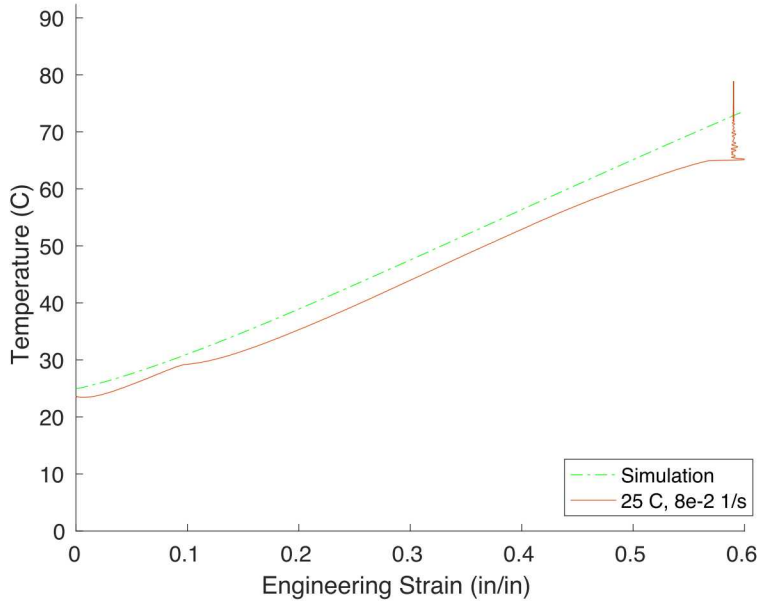

(b)

Figure 2: Comparison of measurements and predictions for the room temperature tests at a strain rates of 2×10^{-4} and 8×10^{-2} s^{-1}. (a) Engineering stress-strain and (b) temperature-strain for the faster strain rate.

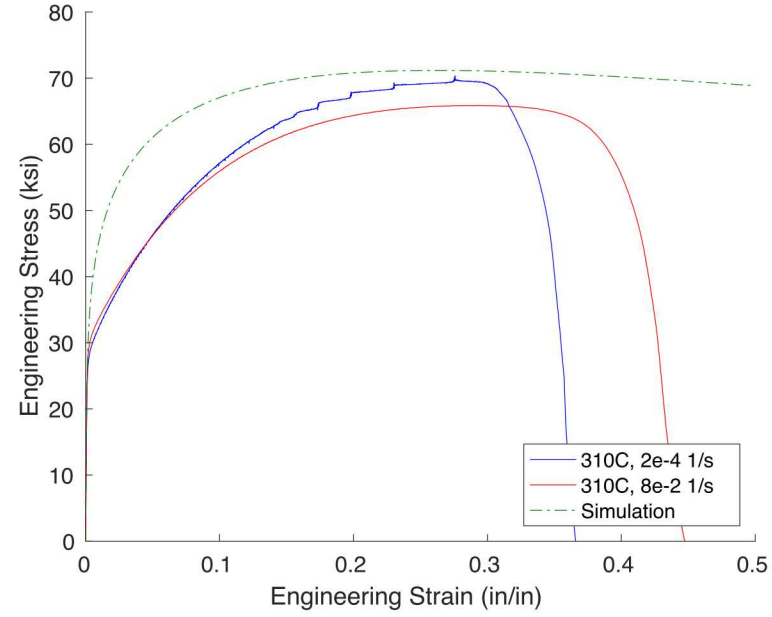

(a)

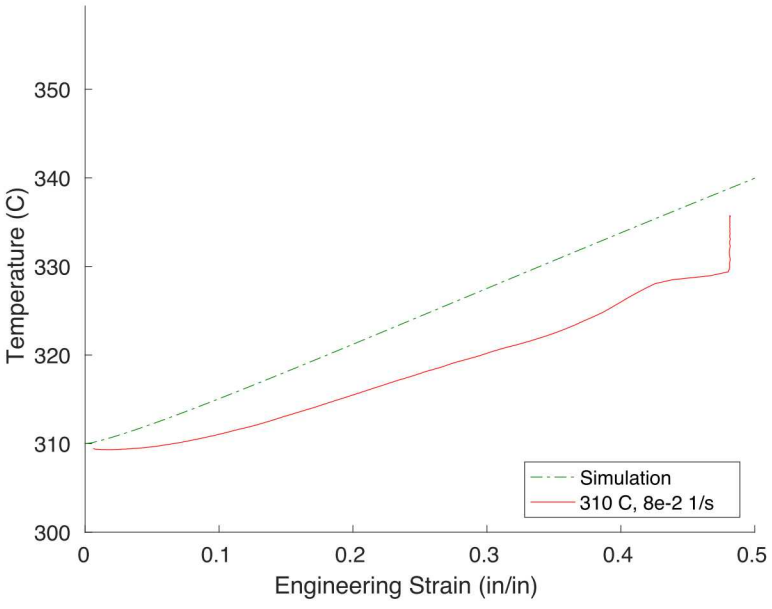

(b)

Figure 3: Comparison of measurements and predictions for the tests at 310°C and strain rate of 2×10^{-4} and 8×10^{-2} s^{-1}. (a) Engineering stress-strain and (b) temperature-strain for the faster strain rate.

is the power-law hardening expression in (1) with its three parameters being functions of temperature and

$$R = R(\dot{\varepsilon}_t^p, T) = 1 + C(T) \ln \left(\frac{\dot{\varepsilon}_t^p}{\dot{\varepsilon}_o} \right) \tag{7}$$

is the Johnson-Cook form for rate dependence, where the calibration constant C can also be a function of temperature. The true stress increment is then given by

$$d\sigma_t = H dR + R dH, \tag{8}$$

where

$$dH = \frac{\partial H}{\partial \varepsilon_t^p} d\varepsilon_t^p + \frac{\partial H}{\partial T} dT \tag{9}$$

and

$$dR = \frac{\partial R}{\partial \dot{\varepsilon}_t^p} d\dot{\varepsilon}_t^p + \frac{\partial R}{\partial T} dT. \tag{10}$$

Finally, the model is adiabatic so that the increase in temperature due to plastic deformation is given by

$$\Delta T = \beta \frac{\int_o^{\varepsilon_t^p} \sigma_t d\varepsilon_t^p}{\rho \bar{C}} \tag{11}$$

where β is the Taylor-Quinney parameter to be calibrated, ρ is the density of the material and $\bar{C}$ is the heat capacity.

In order to calculate A, B and n as functions of temperature, the data in Table 1 was interpolated using a quadratic fit, as shown in Fig. 4. The parameters are plotted in terms of the homologus temperature

$$\hat{T} = \frac{T - T_{\text{ref}}}{T_{\text{melt}} - T_{\text{ref}}} \tag{12}$$

where T_{ref} is a reference temperature taken as 25°C and T_{melt} is the melting temperature taken as 1400°C. The range of applicability of the fit does not extend beyond 310°C ($\hat{T} > 0.2$) but the temperatures considered here did not rise much past that value. The value of ρC was 562 lb-in/(in^3 $-^\circ$ C)

Figure 5 shows a comparison between the numerical results in Fig. 1 to those obtained with the simple model. The results match very well up to the ultimate stress. Recall that the results of the model become invalid past this point. The results at high temperature are slightly different due to the time step dependence of the simple procedure used.

The engineering stress-strain results from the simple model for the fast loading rate at 25°C are shown in dot-dashed line and compared to the measurements in Fig. 2(a). Several cases are shown as the different components of the model are activated:

- Without strain dependence nor adiabatic heating, the predicted response matches the slow test (black line).

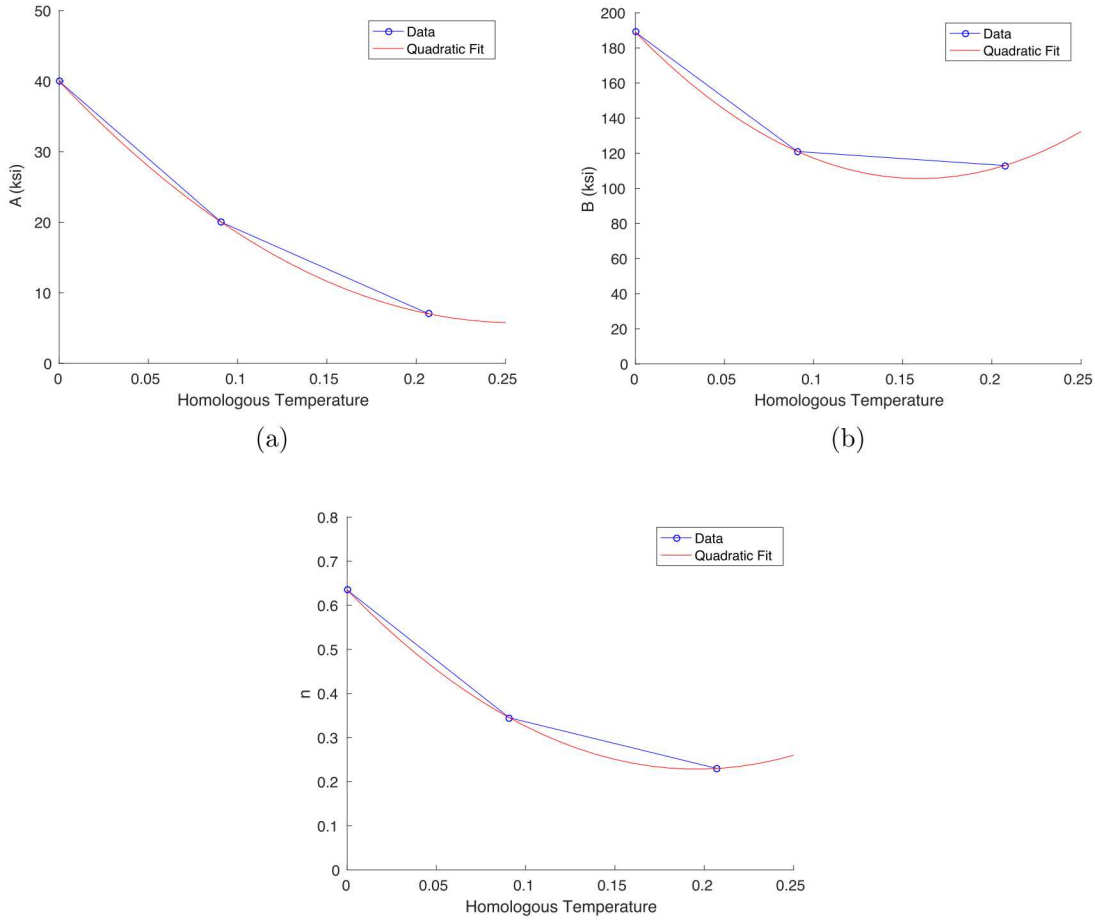

Figure 4: Variations of the power-law hardening parameters with temperature and quadratic fits. (a) A, (b) B and (c) n.

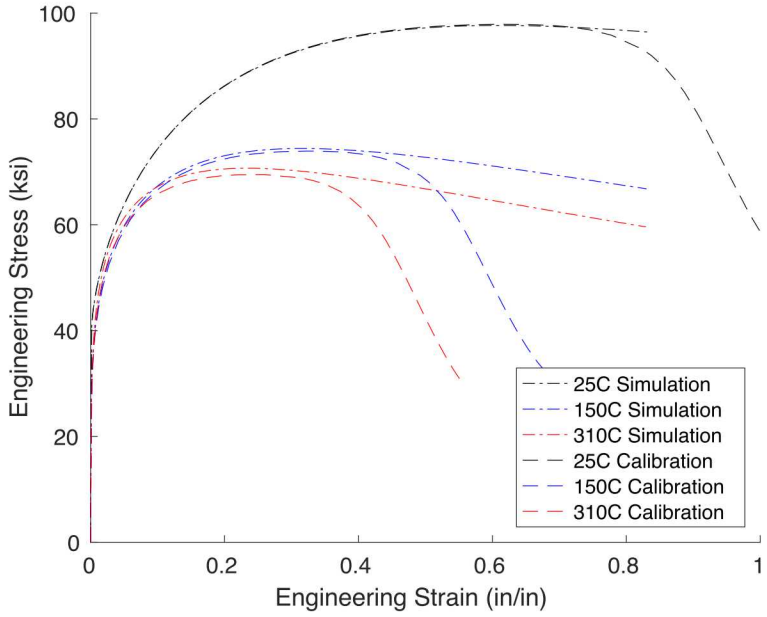

Figure 5: Comparison of the engineering stress-strain responses from the calibration conducted by simulating the geometry of the tension test (calibration) and the responses from the material-point calculations (simulation).

- Setting the strain rate parameter C to 0.0209 causes the intial yield to rise to the level in the tests, but subsequently overpredicts the stress significantly (blue line). It also overestimates the strain at the ultimate stress.
- Setting the percent of plastic work converted to heat (β) to 0.6 gives a response that is closer to the test data (red line). This value was chosen based on matching the measured temperature rise at the center of the specimen. The strain at ultimate stress is more in-line with the test data.
- Adding a linear variation of C so it goes from 0.0209 at room temperature to 0 at 310°C gives a curve that is slightly closer to the test results (green line).
- Figure 2(b) shows the predicted temperature as function of engineering strain for the last case.

Figure 3(a) compares the engineering stress-strain results from the model to the test measurements at 310°C. There is very little change between the results since the value of the strain rate coefficient C goes to zero at 310°C and the temperature rise is relatively mild as shown in Fig. 3(b). In these calculations the fraction of plastic work converted to heat was reduced from 0.6 to 0.5 to better match the temperature measurements. Note that the main reason for the temperature difference between simulation and test is due to the much flatter inital slope of the measurements. This is partly due to the overestimation of the stress in the simulations, but it may also be a consequence of fixing the value of β for the whole

simulation. Recent measurements have shown this to not be the case (Jones et al, 2018) and will be briefly described in the next section.

2 Plastic Work Fraction Converted to Heat in 304L Stainless Steel

The objective of this work was to measure the fraction of plastic work that is converted to heat (Taylor-Quinney parameter, β), for 304L stainless steel specimens from the same stock as were used in the previous section. Funding for the experiments was provided via an Express LDRD (Amanda Jones, PI), and funds from this project helped to finalize the data analysis and provided the final measurements of β from uniaxial tension tests. The results yielded β as a function of strain for two initial temeperatures and strain rates. This data is important for V&V efforts because it provides essential information to validate the results of thermal-mechanical models, especially under high rates of deformation when isothermal models are not adequate.

The results of the effort as well as the description of the experiments and data reduction have been documented in detail by Jones et al (2018). The principal results are shown in Fig. 6 which is reproduced from their report. The plots show the Taylor-Quinney coefficent β as function of the true plastic strain in the uniaxial tension tests. Results are shown for two ambient temperatures and two strain rates. The results for the faster strain rate are shown in solid line and have significantly less uncertainty than those for the slower strain rate. The main reason is that the thermal conduction, convection and radiation effects are relatively minor due to the short duration of the test. The results show β increasing with true plastic strain in all cases.

Note that for the room temperature (RT) test with strain rate of 8×10^{-2} s^{-1}, β varies from 0.55 to 0.8 over the strain range in the test. Therefore, the value used in the simulations in Fig. 2(b), $\beta = 0.6$ is within the range of the measurements. For the test at 250°C at the same rate on the other hand, β varies from about 0.35 to 0.72. The value used for the results in Fig. 3(b), with ambient temperature of 310°C, was $\beta = 0.5$. That figure showed that the temperature rise was initially faster in the model. The rate of temperature increase seen in the tests increased with strain. This correlates, at least qualitatively, well with the increase in β seen in Fig. 6. The curves for the slower strain rate follow similar trends, but note that β goes above one for the room temperature test, thus demonstrating the higher level of uncertainty in the data reduction for the slow tests.

In conclusion, the measurements of β help validate the results obtained in Section 1. They also provide motivation to incorporate material models where β can be a function of strain, strain rate and temperature in thermal-mechanical analyises, provided that calibration data is available.

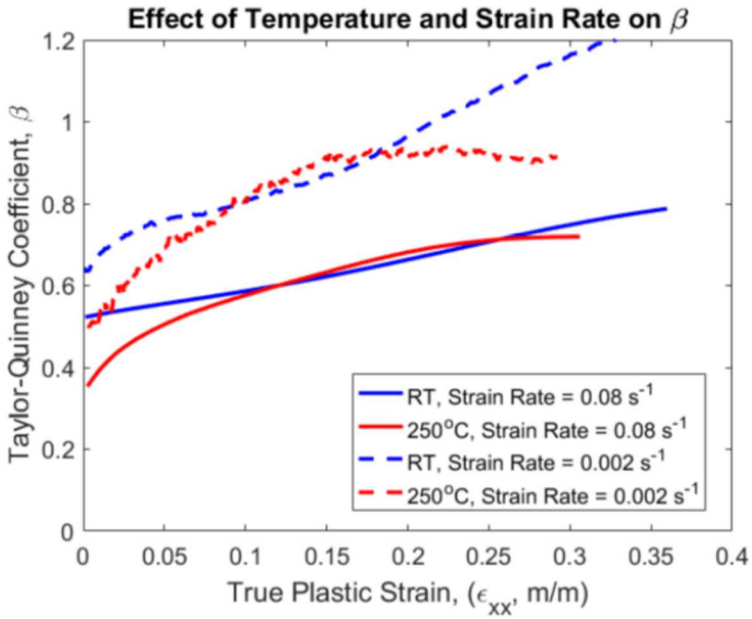

Figure 6: Taylor-Quinney coefficent measurements by Jones et al (2018).

3 Kinematic Hardening Models for Crush-Pressurization and Drop Scenarios

3.1 The Bauschinger Effect

Problems in metal plasticity that involve reversed loading are generally best treated with kinematic hardening models since they can represent the Bauschinger effect. Figure 7 illustrates this phenomenon using a schematic of a uniaxial stress-strain curve. Upon loading from O the material is linearly elastic until the yield point A. Suppose the loading continues to point B where the stress is σ_b and then it is reversed so the material first unloads elastically, yields again at point C and continues loading into the plastic range again. The Bauschinger effect refers to the observation that the yield stress at C is smaller in absolute value than the initial yield stress at A. In other words, $|\sigma_o'| < \sigma_o$. The commonly used isotropic hardening model, with its expanding yield surface, actually predicts that yielding under reverse loading would not occur until $\sigma = -\sigma_b$, therefore greately oversetimating the size of the elastic region. Kinematic hardening on the other hand, keeps the original size of the yield surface constant and hardening is accomodated by translation of the yield surface. It can therefore account for the Bauschinger effect (see also Fig. 3 in Corona, 2018). The next two examples compare structural responses as predicted by isotropic an kinematic hardening models.

3.2 Container Crush Followed by Pressurization

Figure 8 shows a schematic of this problem. It consists of a cylindrical container with diameter and length of 3 in. and uniform thickness t laterally crushed first between two rigid

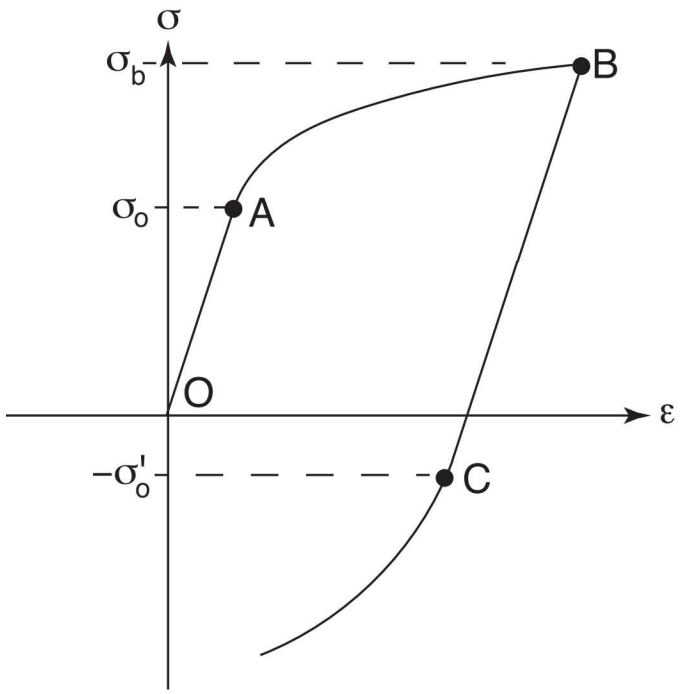

Figure 7: Bauschinger effect: Upon reverse loading from point B the material yields at point C such that $|\sigma_o'| < \sigma_o$.

plates by moving the top plate down by a distance $\Delta = 0.25$ in. after first contact. Following crush, the can is pressurized internally until the pressure reaches $P = 1000$ psi. The material is taken to have Young's modulus and Poisson's ratio $E = 30 \times 10^6$ psi and $\nu = 0.3$. The yield stress is $\sigma_o = 40$ ksi and the hardening modulus is a constant $E_t^P = 260$ ksi. The density of the material was taken as 0.29 lb/in^{-3}.

This example clearly calls for the exploration of kinematic hardening due to the nature of the load sequence. Cases with two different thicknesses will be considered: $t = 0.020$ in. and $t = 0.080$ in. Figure 9 shows the calculated displacements at two points described in the insert for the case with $t = 0.02$ in. These calculations were conducted using Abaqus/Explicit with shell elements of type S4R.

Crushing was applied in 10 ms followed by pressurization also in 10 ms. Figure 9(a) shows the calculated displacements during crush. The isotropic hardening results are shown in solid line while the kinematic hardening results are shown in dashed line. Note that although the results from isotropic and kinematic hardening are close, they are not identical. This can happen due to local unloading or reloading at some points of the container during crush, or to the non-proportionality of the stress trajectories, which can also make the calculated responses of the two models to differ. This was not investigated further in this example. Figure 9(b) shows the motion of the same two points during pressurization. At the start of pressurization, the compression plate is removed from the model, so oscillations in both

displacements can be seen at low pressure. Whereas D_A increases smoothly, point D_b shows a relatively sudden jump at approximately 200 psi. In any case, the results from both isotropic an kinematic hardening are very similar for this thickness. Since thin shells are less influenced by material plastic behavior, it is worth investigating the case when the container thickness is a factor of 4 larger.

Figure 10 shows similar results for a can with $t = 0.08$ in. There is little diference between the predictions of the two models during crush as seen in Fig. 10(a). More significant differences between the results calculated by the isotropic and kinematic hardening models occur during pressurization. Both models predic a sudden increases for both D_a and D_b, but while the jumps for the isotropic hardening model occur at about 900 psi, those for the kinematic hardening model occur just before 600 psi. If the quantity of interest was the container configuration bewteen 600 and 800 psi, for example, the two models give very different answers.

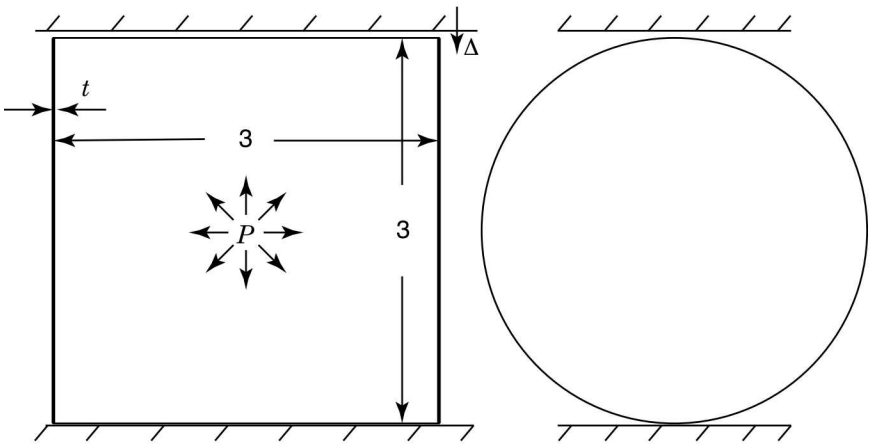

Figure 8: Geometry for the can crush exercise.

3.3 Can Drop

In the second scenario that will be used to compare the results of isotropic and kinematic hardening it is perhaps less obvious that significant differences between the two models would be apparent. The scenario is described schematically in Fig. 11. It consists of a an outer circular cylindrical container. A second cylindrical shell resides inside the first, carries a 2.6 lb mass at its forward end and is attached in cantilever fashion to the base of the outer container at the other. The whole assembly is tilted at $\theta = 30^\circ$ and impacts a rigid surface with velocity $V = 431$ in/s. The quantity of interest is the equivalent plastic strain induced at the junction between the inner and outer cylinders. The simulation is carried out for 5 ms, which is sufficient for the container to impact the ground first on the left and then on the right.

Figure 12(a) shows the case when a material with the same elastic and yield properties as in the previous case, but with very low hardening modulus $E_t^p = 30$ ksi is used. The maximum

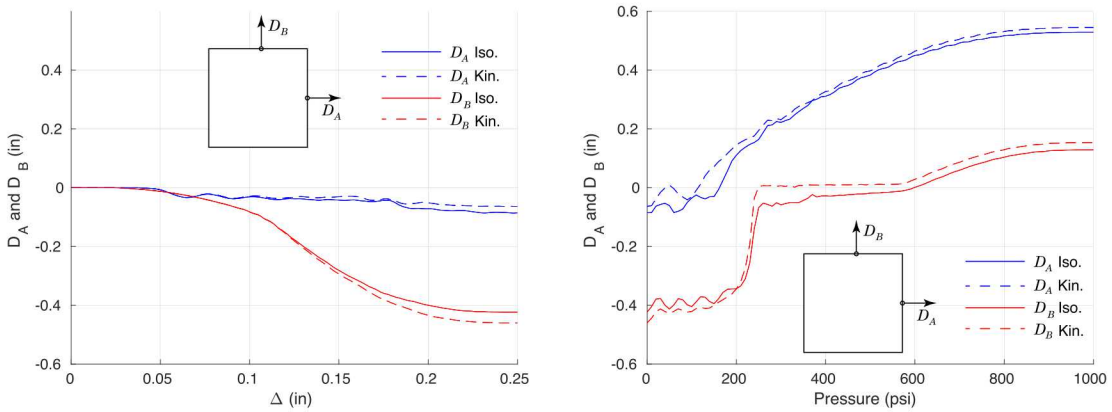

(a) (b)

Figure 9: Displacements at two points during deformation of a can with $t = 0.020$ in. (a) During crush and (b) during pressurization.n

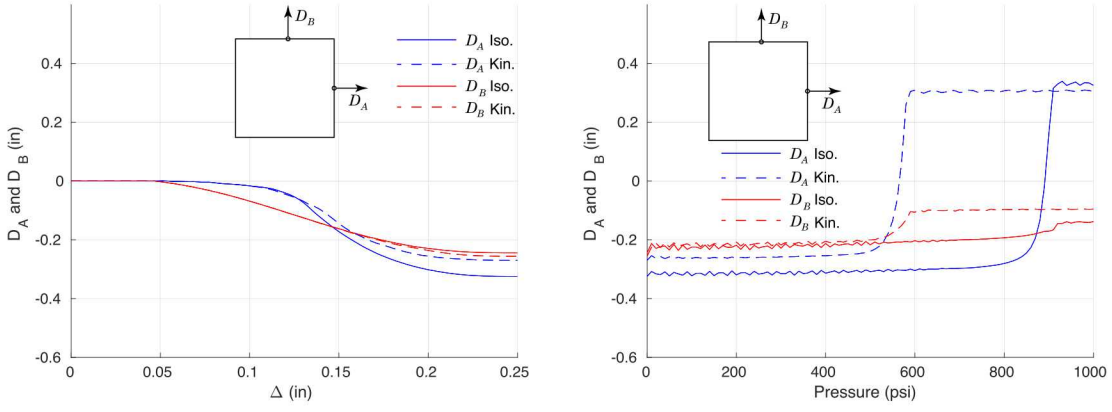

(a) (b)

Figure 10: Displacements at two points during deformation of a can with $t = 0.080$ in. (a) During crush and (b) during pressurization.

equivalent plastic strain occurred at location A, and is plotted against time. The isotropic and kinematic hardening results are indicated in the figure. At times, only the accumulation of plastic strain when the stress triaxiality in the material is positive is considered to determine whether material failure may occur. Therefore, triaxiality information is included in the figures by the color of the lines. Green means that the triaxiality is zero or negative while red means that the triaxiality is positive. Note that the initial jump in equivalent plastic strain at first impact is essentially the same for both models. The susequent relative motion of the inner container with respect to the outer is enough to induce plastic defomration and causes the plastic strain to continue to increase. During this time the container is rotating so as to decrease the angle θ. A second jump in plastic strain a little after 3 ms occurs when the front of the container strikes the rigid surface. The jump predicted by the kinematic hardening model at this time is somewhat larger than the one by the isotropic hardening model. All in all, the differences are not that great. This is mostly due to the low hardening modulus of the material.

Bigger differences can occur for high hardening materials, as shown in Fig. 12(b) where $E_t^p = 660$ ksi. Althought the overall plastic strains are smaller in this case, the difference between the predictions by the two material models is much more striking (twice as much plastic strain predicted by kinematic vs. isotropic hardening) indicating that in this class of impact problems it may be prudent to consider the use of kinematic hardening models. Finally, Fig. 13 shows the configurations as predicted by both models at the end of the simulation. No major differences can be appreciated at this level even though the kinematic hardening model predicted significantly higher plastic strains at point A. (The contours of equivalent plastic strain shown are from the opposite side of the shell from which the results in Fig. 12 were obtained).

4 Summary and Conclusions

This memo summarized the activities undertaken during FY2018 for the project on V&V of Thermal-Mechanical Failure. It was divided into three parts. The first demonstrated that to capture the behavior exhibited by 304L stainless steel at different strain rates and temperatures it is necessary to include a significant amount of complexity in the material model, even if it is based on classical plasticity. In particular, the shape of the hardening function changes with temperature, which in the current work was accommodated by making the parameters of a power-law hardening model functions of temperature. Furthermore the rate-dependence of the material response also has to be accounted for. This was accomplished by introducing a Johnson-Cook-like rate dependence with the rate dependence term being a function of temperature as well. Finally, for the high strain rate tests considered here, including adiabatic heating of the specimen was necessary. Based on this model, the fraction of plastic work converted to heat (Taylor-Quinney parameter, β) was set to 0.6 when the initial temperature was at 25°C and to 0.5 when the initial temperature was 310°C to match the experimental measurements.

The second part addressed the measurement of the Taylor-Quinney parameter for the same

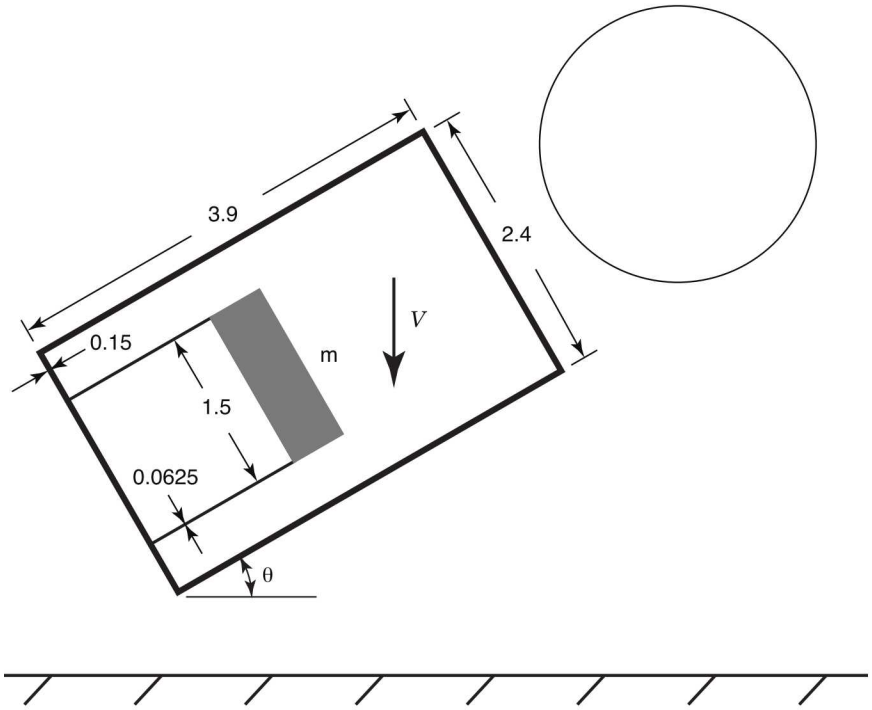

Figure 11: Geometry for the can drop exercise.

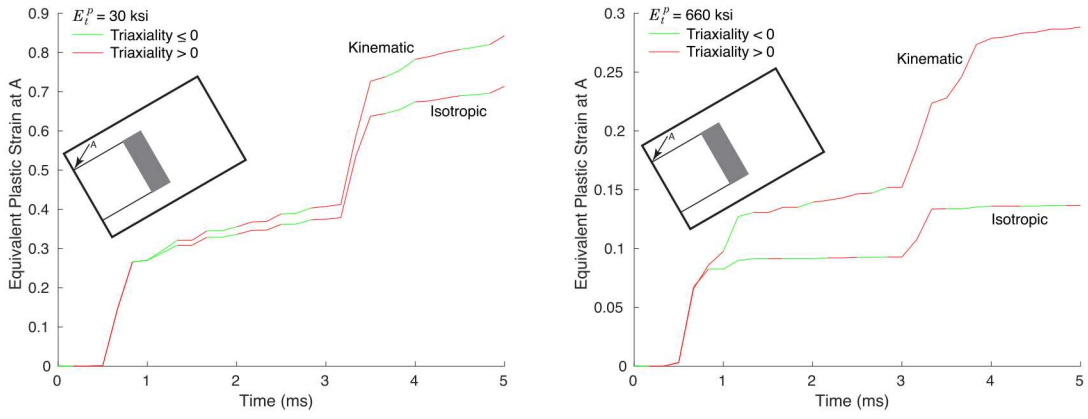

(a) (b)

Figure 12: Equivalent plastic strain measured at point A during impact. (a) For a low hardening material with $E_t^p = 30$ ksi and (b) for a higher hardening material with $E_t^p = 660$ ksi.

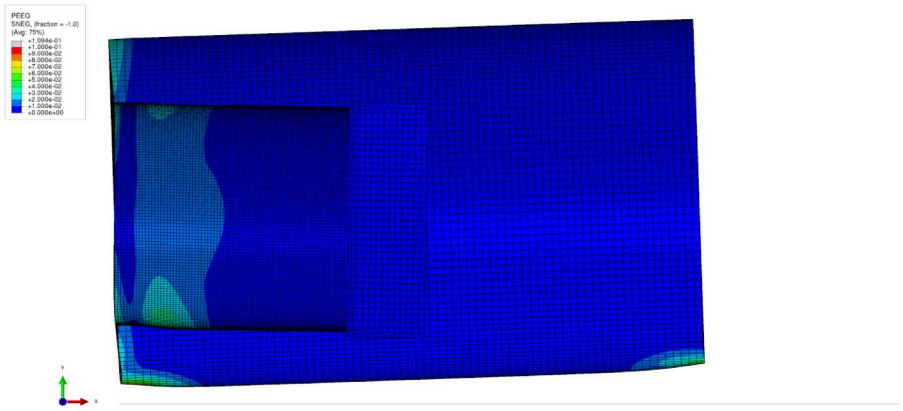

(a)

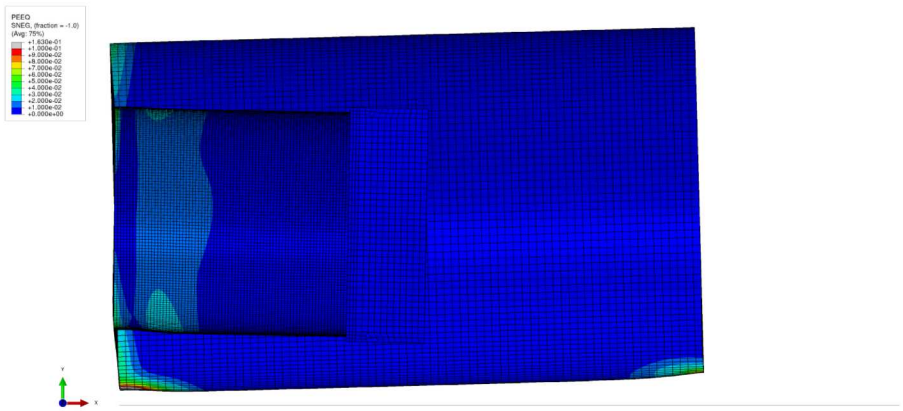

(b)

Figure 13: Final configurations of the can drop problem at time of 5 ms with contours of equivalent plastic strain. (a) Isotropic hardening model and (b) kinematic hardening model.

material. It was found that under uniaxial stress loading, the value of the parameter depended on the values of temperature, strain rate and strain. In general the parameter increased with strain but its initial value decreased with temperature and strain rate. For the lower, quasi-static rate considered, the tests were essentially isothermal, and the uncertainty in the measured trends is significant.

The third part of the report addressed comparisons between isotropic and kinematic hardening plasticity models for two problems: crush of a can followed by internal pressurization and a drop scenario involving a cylindrical can that included an internal component in the form of a smaller, cantilevered cylindrical shell that carried a weight at its free end (Fig. 11). The first problem obviously includes load reversals at the material level and one can expect significantly different predictions between kinematic and isotropic models. The results show that this is indeed the case, although the degree to which the results can differ depends on the parameters of the problem. It is perhaps less intuitive that the drop scenario could involve load reversals large enough for the results to display significant differences between isotropic an kinematic models. The results show significant differences between the models when looking at the accumulated equivalent plastic strain at a critical point in the geometry. The results therefore point to a need to evaluate predictions by kinematic hardening models when looking at drop scenarios or problems that involve sequential loading.

Sandia National Laboratories is a multimission laboratory managed and operated by National Technology & Engineering Solutions of Sandia, LLC, a wholly owned subsidiary of Honeywell International Inc., for the U.S. Department of Energy's National Nuclear Security Administration under contract DE-NA0003525.

References

Corona, E. (2018) "Dynamic, elastic-plastic response of 2-DOF mass-spring system," Memo to M. Guthrie, SAND2018-1809R.

Corona, E. and Lester, B. (2017) "V&V of Thermal-Mechanical Failure–FY2017: Failure of a Laser-Welded Pressurized Container," Memo to distribution, SAND2017-11141R.

Jones, A. (2018). "SML4181-Thermomechanical Testing, 304L Base Material and Laser Welds," Memo, May, 2018.

Jones, A., Jones, E., Reedlunn, B. and Kramer, S. (2018) "Conversion of Plastic Work to Heat: A Full-Field Study of Thermomechanical Coupling," Sandia Report SAND2018-10763.

Internal Distribution:

R. Hogan	1510
E. Jones	1512
S. Burns	1514
D. Jones	1528
S. Kramer	1528
K. Dowding	1544
M. Guthrie	1553
E. Fang	1554
B. Reedlunn	1554
W. Scherzinger	1554
D. VanGoethem	1554
J. Emery	1556
B. Antoun	8343
K. Karlson	8752